Feasibility Study for the Improvement of Microcalcification Visualization in Different Breast Thicknesses and Tissue Components Using a Dual-Energy Approach in Digital Mammography

Chia-Jung Tsai, PhD, Ran-Chou Chen, MD,*† Shuo-Hui Hung, PhD,*‡ Jay Wu, PhD,§ Hui-Ling Peng, MD,|| and Jason J.S. Lee, PhD**

Objective: The purpose of this study was to improve detectability of microcalcifications using a dual-energy digital mammographic (DEDM) technique.

Methods: Slabs of uniform breast-equivalent plastic and an additional plate were used to mimic various breast thicknesses, from 3 to 7 cm, and to simulate microcalcification with diameters from 0.16 to 0.39 mm. Free-response receiver operating characteristics and area under the curves (A_z) were used to evaluate the sensitivity of detecting microcalcifications using the DEDM compared with using the conventional single-energy digital mammography (SEDM).

Results: The mean number of false-positives per image was 0.0198 ($A_z = 0.956 \pm 0.027$) using DEDM compared with 0.292 ($A_z = 0.681 \pm 0.235$) using SEDM. A lower radiation dose could be possibly obtained for the DEDM technique with a thickness of less than 5 cm compared with the SEDM with a thickness larger than 5 cm.

Conclusions: Microcalcifications could be more accurately and efficiently detected using the DEDM, which might bring reliable and promising applications on early computer-aided diagnosis of breast cancer.

Key Words: microcalcification detection, digital mammography imaging, dual-energy imaging

(*J Comput Assist Tomogr* 2012;36: 488–494)

Because microcalcifications are one of the earliest indicators of breast cancer, a leading cause of mortality in women,[1] their detection at an early stage plays a decisive role in reducing the mortality. The full-field digital mammography (FFDM) has been the criterion standard for breast cancer screening.[2,3] Microcalcifications, composed primarily of calcium compounds such as apatite, calcium oxalate, and calcium carbonate, have a higher x-ray attenuation coefficient than the surrounding normal breast tissue.[4] However, when small microcalcifications (<1 mm) are overlapped with different tissues (eg, adipose, glandular tissue, ducts and masses), it becomes difficult to detect a breast lesion even when the signal-to-noise ratio (SNR) is high.[5] Moreover, scattered radiation is one major intrinsic problem for the FFDM system, which reduces SNR and subject contrast in the image, thus degrading the image quality and detectability of any microcalcification. Currently, the most widely used method for reducing scattered radiation is the antiscatter grid, but for FFDM, with a wide exposure latitude, the cost of using a grid is a reduction of the SNR due to loss of primary x-rays. Therefore, improving SNR or contrast in the FFDM especially for microcalcification is worth exploring for the earlier detection of breast diseases.

In recent decades, studies for improving microcalcification visualization have used several postprocessing imaging tools such as wavelet analysis,[6,7] classic image filtering,[8] stochastic fractal models,[9] and multiscale analysis.[10] Dual-energy digital mammography (DEDM) was proposed to be a promising technique that can improve the detection of microcalcifications. It involves acquiring 2 images of the subject by using 2 x-ray spectra to exploit the difference in the energy dependence of x-ray attenuation between different materials. By properly combining the low- and high-energy images, one type of object from the image is enhanced, whereas others may be cancelled or reduced.

Although the DEDM technique has been proposed in the evaluation of breast tumors,[11] its application for the detection of microcalcifications was limited owing to the inherently low contrast of microcalcifications and high background noise in the subtracted image.[12] Most of the current DEDM techniques used a weighted subtraction tool, with a linear combination of logarithmic low- and high-energy images to generate a subtracted image,[5,13,14] consisting of residual tissue structures that would severely reduce the image contrast.

Kappadath and Shaw[15] investigated this effect with various inverse-map functions on the DEDM, and they concluded that a mean fitting error of ~50 μm and that a max filtering error of ~150 μm could be obtained for a given microcalcification thickness using cubic and conic functions (nonlinear). An alternative was proposed by using a scatter and nonuniformity correction model for the DEDM,[16] and it indicated that sizes of microcalcifications could be substantially decreased to 250 to 280 μm with a clinical scanner. However, calcifications smaller than 250 μm were usually not visible in most cases owing to the residual quantum noise.

This study was aimed to develop a DEDM technique for efficiently eliminating quantum noise to improve detectability of microcalcifications, by using a commercially available flat-panel FFDM. Data were acquired using DEDM on various combinations of breast thicknesses and tissue densities using a

From the *Department of Biomedical Imaging and Radiological Sciences, National Yang Ming University; Departments of †Radiology and ‡Surgery, Taipei City Hospital, Taipei; §Department of Biomedical Imaging and Radiological Science, China Medical University, Taichung; and ||Department of Diagnostic Radiology, Shin Kong Wu Ho-Su Memorial Hospital, Taipei, Taiwan.

Received for publication February 3, 2012; accepted April 4, 2012.

Reprints: Ran-Chou Chen, MD, or Jason J.S. Lee, PhD, Department of Biomedical Imaging and Radiological Sciences, National Yang Ming University, Department of Radiology, Taipei City Hospital, 155 Li-Nong St, Sec. 2, Taipei, Taiwan 112 (e-mail: chenranchou@yahoo.com.tw; jslee@ym.edu.tw).

This study was financially supported by the National Science Council of Taiwan (NSC99-2314-B-010-030-MY2).

Copyright © 2012 by Lippincott Williams & Wilkins

Copyright © 2012 Lippincott Williams & Wilkins. Unauthorized reproduction of this article is prohibited.

breast phantom, and results were compared to those of conventional single-energy digital mammography (SEDM).

MATERIALS AND METHODS

DEDM Theory

Lemacks et al[12] proposed a numerical framework to perform the signal calculation in DEDM. They assumed that there were 3 attenuation materials in the breast (adipose tissue, glandular tissue, and microcalcifications), each with an individual thickness of t_a, t_g, and t_c, respectively, corresponding to their linear attenuation coefficients, μ_a (E), μ_g (E), and μ_c (E). Depending on the distribution of materials, the mean measured signals in the high- and low-energy images for microcalcification are given by

$$(S_j)_M = \int R_j \times d^2 \times \Phi_j(E) \times e^{-\mu_a(E)T} \times e^{-\Delta\mu_g(E)t_g - \Delta\mu_c(E)t_c} \times A(E) \times Q(E)\, dE \quad (1)$$

where j = H (ie, high energy), L (ie, low energy). T represents the compressed total breast thickness, R is the unattenuated x-ray exposure at the detector plane, d is the pixel size, and $\Phi(E)$ is the unattenuated photon flux per unit exposure per energy at the detector input. $A(E)$ is the photon absorption ratio of the detector as a function of photon energy, E, and $Q(E)$ is the detector response function that represents the signal generated by each detected x-ray photon as a function of photon energy, E. Defining $\Delta\mu_g(E) \equiv \mu_g(E) - \mu_a(E)$ and $\Delta\mu_c(E) \equiv \mu_c(E) - \mu_a(E)$, referred to as the difference-attenuation coefficients, we solve for t_a.

Similarly, the mean measured signals in the high- and low-energy images for background, $(S_H)_B$ and $(S_L)_B$, can be expressed as:

$$(S_j)_B = \int R_j \times d^2 \times \Phi_j(E) \times e^{-\mu_a(E)T} \times e^{-\Delta\mu_g(E)t_g} \times A(E) \times Q(E)\, dE;\ j = H, L. \quad (2)$$

We assume that the maximum energy of x-ray spectra in the high- and low-energy images is E_1 and E_2, respectively ($E_1 > E_2$). Thus, the mean signal for microcalcifications and for background can be rewritten based on equations (1) and (2), as follows:

For microcalcifications:

$$\begin{aligned}\Delta S_M = {} & \int_0^{E_2} R_L \times d^2 \times \Phi_L(E) \times \frac{R_H \Phi_H(E)}{R_L \Phi_L(E)} \\ & \times e^{-\mu_{aL}(E)T} \times e^{-\Delta\mu_{gL}(E)t_g - \Delta\mu_{cL}(E)t_c} \\ & \times e^{\left(\frac{\mu_{aH}(E)}{\mu_{aL}(E)} + \frac{\Delta\mu_{gH}(E)}{\Delta\mu_{gL}(E)} + \frac{\Delta\mu_{cH}(E)}{\Delta\mu_{cL}(E)}\right)} \\ & \times A(E) \times Q(E) \times dE + \int_{E_2}^{E_1} R_H \times d^2 \\ & \times \Phi_H(E) \times e^{-\mu_{aH}(E)T} \times e^{-\Delta\mu_{gH}(E)t_g - \Delta\mu_{cH}(E)t_c} \\ & \times A(E) \times Q(E) \times dE + \int_0^{E_1} R_L \times d^2 \times \Phi_L(E) \\ & \times e^{-\mu_{aL}(E)T} \times e^{-\Delta\mu_{gL}(E)t_g - \Delta\mu_{cL}(E)t_c} \\ & \times A(E) \times Q(E) \times dE \equiv c_1 \times (S_H)_M + d_1 \end{aligned} \quad (3)$$

For background:

$$\Delta S_B \equiv c_2 \times (S_H)_B + d_2 \quad (4)$$

where c_1 and c_2 are constants

$$d_1 = \left[\frac{R_H \Phi_H}{R_L \Phi_L} e^{\left(\frac{\mu_{aH}}{\mu_{aL}} + \frac{\Delta\mu_{gH}}{\Delta\mu_{gL}} + \frac{\Delta\mu_{cH}}{\Delta\mu_{cL}}\right)} - 1\right](S_L)_M$$

and

$$d_2 = \left[\frac{R_H \Phi_H}{R_L \Phi_L} e^{\left(\frac{\mu_{aH}}{\mu_{aL}} + \frac{\Delta\mu_{gH}}{\Delta\mu_{gL}}\right)} - 1\right](S_B)_M$$

We can express equations (3) and (4) as the signal difference between high-energy and low-energy images (ie, the

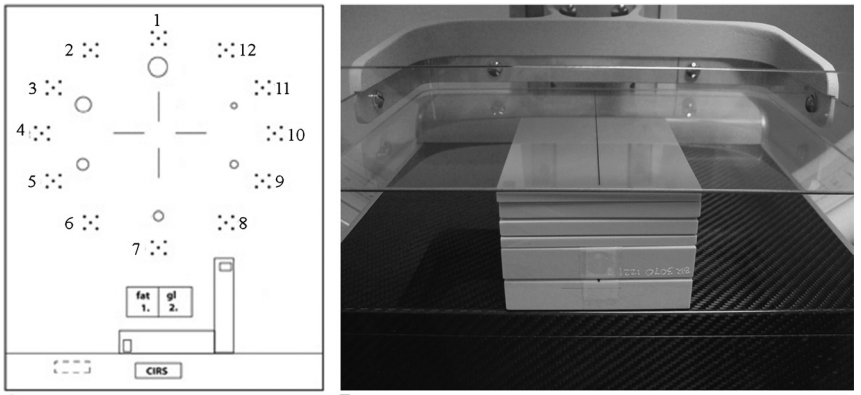

FIGURE 1. A, Stimulated microcalcification phantom in which numbers 1 to 6 were made from calcium carbonate ($CaCO_3$) and numbers 7 to 12 were from aluminum (Al). B, Photograph showing the phantom position with overlapped normal tissue component plate stimulating different breast thickness conditions with varied tissue densities.

© 2012 Lippincott Williams & Wilkins

Copyright © 2012 Lippincott Williams & Wilkins. Unauthorized reproduction of this article is prohibited.

subtracted image), which is equal to the signal at the high-energy multiplied by a ratio of c_1, in which integrated energy from E_2 to E_1, and add a constant representing a ratio of $\frac{R_H\Phi_H}{R_L\Phi_L}e^{\left(\frac{\mu_{aH}}{\mu_{aL}}+\frac{\Delta\mu_{gH}}{\Delta\mu_{gL}}+\frac{\Delta\mu_{cH}}{\Delta\mu_{cL}}\right)}-1$ of the low-energy signal. Thus, we can denote the signal difference for microcalcifications as a linear correlation with the signal at high-energy, $(S_H)_M$, with a slope of c_1 and a y intercept of d_1. Likewise, the signal difference for background also can be denoted as $c_2 \times (S_H)_B + d_2$. In accordance with this DEDM theory, the maximum information concerning microcalcifications and background can be identified through the proposed algorithm.

Breast Phantom

A plate consisting of 6 different sizes of presifted calcium carbonate grains and aluminum grains (Computerized Imaging Reference Systems [CIRS], Inc, Norfolk, Va) was used to simulate microcalcifications with diameters of 0.39, 0.27, 0.23, 0.20, 0.16, and 0.13 mm, as shown in Figure 1A in order from number 1 to number 6. Each cluster contained 5 microcalcifications of the same size to ensure measurement reproducibility. Because of the limited visibility of the mammography system for a pixel size less than 85 μm, we excluded 0.13-mm-sized microcalcifications from this experiment. Moreover, although the feasibility of using aluminum grains as just-visible microcalcifications for the FFDM system had been already proven,[17] we excluded the aluminum grains as microcalcifications to simplify our experimental parameters.

To realistically mimic breast imaging conditions, slabs of breast-equivalent plastic (CIRS, Inc), with densities simulating 70%, 50%, and 30% adipose (corresponding to 30%, 50%, and 70% glandular tissue, respectively) were used to achieve various breast thicknesses. Thin breasts were composed of 3-, 3.5-, 4-, and 4.5-cm thicknesses and thicker breasts were represented by slabs with thicknesses ranging from 5, 6, and 7 cm. During image acquisition, a plate containing varying sizes of microcalcifications was placed on top of a 20-mm-thick slab with 1 edge aligned to the edge of the chest wall. Additional slabs composed of 30%, 50%, or 70% adipose tissue were then stacked on top to simulate glandular breast tissue of varying thicknesses (Fig. 1B). The breast phantom was maintained at a fixed height and position so its image always occupied the same size and position on the detector array. This made the subsequent region-of-interest (ROI) analysis easier to perform.

Image Acquisition Using DEDM and SEDM

Screening with the FFDM system (Giotto Image System; IMS, Bologna, Italy) was performed with a direct flat-panel detector, consisting of a semiconductor layer of amorphous selenium (Se) placed under a direct current before x-ray exposure. The absorption of x-rays caused local charge equalization. The charges were captured by an array of electrodes, storage capacitors, and transistors located behind the Se layer and were converted to electronic signals. After electronic enhancement and analog-to-digital signal conversion, the digital image was sent to the imaging computer.

Matrix size of the detector was 3584 × 2816, corresponding to a field size of 30.4 × 23.9 cm^2, with a pixel size of 85 μm. Fixed conditions included a 0.3-mm focal spot, a source-to-image distance of 660 mm, compressed paddle with stress of 5 kg (10 lb), and anode/filter of tungsten/silver.

For the DEDM technique, an automatic exposure control was used to acquire each high-energy image at different tissue densities with various breast thicknesses (Table 1). A corresponding low-energy image was achieved by adjusting the tube voltage to its lowest setting, 23 kV (peak), while keeping the effective tube current time product (mA s) the same as that used in the high-energy image acquisition.

TABLE 1. Tube Voltage/Tube Current Time Product (kV [peak]/mA s) Parameter Settings at Different Breast Thicknesses and Tissue Densities in High-Energy Digital Mammography

Thickness, cm		g30/a70	g50/a50	g70/a30
Thinner	3	25/56	25/59	25/62
	3.5	26/54	26/58	26/60
	4	27/55	27/60	27/63
	4.5	28/58	28/64	28/69
Thicker	5	29/63	29/71	29/76
	6	30/87	30/100	30/111
	7	31/120	31/139	31/158

g30/a70 indicates tissue density with glandular of 30% and adipose of 70%; g50/a50, tissue density with glandular of 50% and adipose of 50%; g70/a30, tissue density with glandular of 70% and adipose of 30%.

This study also used SEDM to be the control, acquiring images at the same exposure setting as that in the high-energy acquisition in the DEDM. Two radiologists with more than 5 years of clinical experience have individually reviewed the SEDM images on an image workstation with a 1600 × 1200 resolution, a window/level adjustment and zooming, if necessary. During the review process, the radiologists were not given the phantom information to select ROIs of suspicious microcalcifications by they the recorded their sizes.

Mean glandular dose (MGD), the average value of the absorbed dose in the glandular tissue, was also used to estimate the dose risk. It can be calculated from the following equation:

$$\mathrm{MGD} = \mathrm{ESE} \times D_{\mathrm{gN}} \quad (5)$$

where ESE (entrance skin exposure) is expressed in roentgens (R) and D_{gN} is the normalized dose conversion factor (mGy/R) that resulted from an incident exposure in air of 1 R, being a function of breast density, breast thickness, x-ray beam quality (ie, tube potential and beam half value level), and anode/filter combination.

Statistical Analysis

The acquired images were analyzed using MATLAB software (version 7.10.0.499; MathWorks, Natick, Mass). For each different tissue density, we measured the mean diameter of the microcalcifications for each thickness using the DEDM technique (as stated in Section II.1, DEDM theory). Analysis of variance and Student t test (version 10.0; SPSS, Inc, Chicago, Ill) were performed to compare statistical differences for each microcalcification size and for each tissue density on thinner versus thicker breasts in the DEDM. We also conducted multiple-reader analysis using the Pearson correlation in the SEDM to have consistent agreement between readers and to provide more robust confidence in the readers' evaluations.

To evaluate the accuracy of detection of microcalcifications, we measured free-response receiver operating characteristic (FROC) curves by measuring TP fractions with associated average FP numbers per image. The TP fraction refers to the true-positive detection fraction, which shows how many real microcalcifications can be detected; and the average number of FP per image refers to a false-positive number. A total of 175 ROIs

© 2012 Lippincott Williams & Wilkins

Copyright © 2012 Lippincott Williams & Wilkins. Unauthorized reproduction of this article is prohibited.

for each tissue density were used for the DEDM technique and for comparing it to the SEDM. Each ROI was composed of 5 microcalcifications per diameter × 5 diameters per thickness × 7 thicknesses. Here, a TP fraction of 1 was defined as a detected microcalcification that was overlapped with more than 50% of the suspicious area,[18] and all other microcalcifications were considered FP clusters. A cluster was defined as a group of microcalcification of 2 pixels or more. In addition, areas under the FROC curve (A_z) were also used to compare the accuracy of detectability of microcalcification between the 2 methods. Student t test was performed to compute P values to assess the statistical differences in A_z between the 2 techniques ($P < 0.05$ was considered statistically significant).

RESULTS

In this study, we found that most of the measured microcalcification diameters were greater than the exact values provided by the commercial company (CIRS, Inc; Table 2), with an approximate difference of less than 5 pixels. This was mainly due to the partial volume effect. In comparison of the estimated microcalcification sizes among different tissue densities, there were no significant differences observed (all $P > 0.05$).

In general, the detectability of microcalcification using the DEDM approach showed no correlation between tissue densities of g30/70 and g50/a50. Meanwhile, data for g70/a30 showed slight underestimations especially compared with those of g30/a70, owing to an increased linear attenuation coefficient with increased glandular ratio. On the other hand, there were significant differences in the estimated microcalcification sizes between thinner and thicker breasts for each tissue density.

In the SEDM technique, all estimated microcalcification diameters for 3 tissue densities were plotted in Figure 2 to compare differences on the detected microcalcifications between the 2 professional readers. In the results, the estimated medium diameter of overall performance was 0.50 ± 0.18 mm for reader 1 and 0.41 ± 0.20 mm for reader 2, respectively, and the difference between the 2 readers was less than 2 pixels. Also, there was a good agreement between the 2 readers as evidenced by a Pearson correlation of 0.84 to 0.90.

For the 3 tissue densities in Figure 3, TP fraction was 0.90 for an average of 0.018 to 0.042 FP per image using the DEDM technique compared with an average of 0.134 to 0.422 using the SEDM. In overall performance, the average FP per image was 0.0198 for the DEDM and 0.292 for the SEDM with a TP fraction of 0.90. These results demonstrated that the DEDM technique leads to a more robust estimation of image noise and thereby performed better detection of microcalcification than that with the SEDM technique.

TABLE 2. Estimated Microcalcification Sizes at 3 Different Tissue Densities With Thinner (3–4.5 cm) and Thicker (5–7 cm) Breast Thicknesses

		Estimated Size, mm			
True Size, mm		**g30/a70**	**g50/a50**	**g70/a30**	***P***
Thinner	0.39	0.62 ± 0.05	0.60 ± 0.04	0.59 ± 0.03	0.27
	0.27	0.41 ± 0.03	0.38 ± 0.03	0.36 ± 0.04	
	0.23	0.32 ± 0.02	0.31 ± 0.04	0.29 ± 0.04	
	0.20	0.28 ± 0.02	0.27 ± 0.03	0.25 ± 0.04	
	0.16	0.21 ± 0.04	0.20 ± 0.03	0.18 ± 0.05	
Thicker	0.39	0.57 ± 0.05	0.57 ± 0.03	0.48 ± 0.10	0.10
	0.27	0.34 ± 0.04	0.30 ± 0.09	0.23 ± 0.13	
	0.23	0.23 ± 0.08	0.20 ± 0.08	0.22 ± 0.08	
	0.20	0.18 ± 0.07	0.17 ± 0.08	0.15 ± 0.10	
	0.16	0.14 ± 0.08	0.09 ± 0.07	0.08 ± 0.06	
P		0.001	<0.001	<0.001	

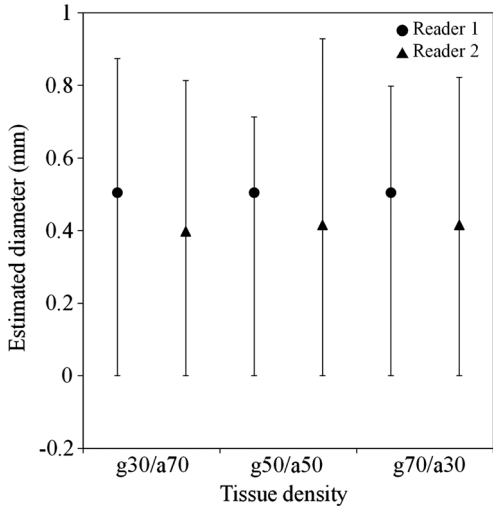

FIGURE 2. Microcalcification diameters were recorded by the 2 readers in SEDM where the medium diameter was marked as ● and ▲, respectively, according to each tissue density. Data showed good agreement between the 2 readers as evidenced by a Pearson correlation of 0.84 to 0.90.

The area under the curves (A_z), obtained as a measure of accuracy of microcalcification detection, were compared with the difference between the DEDM and the SEDM techniques for each tissue density. The estimated A_z values in the DEDM/SEDM methods were 0.948/0.673 for g30/a70, 0.923/0.567 for g50/a50, 0.889/0.627 for g70/a30, and 0.956/0.681 for overall performance, respectively. There were no significant differences in A_z values for various tissue densities using the SEDM method. However, in the DEDM technique, the A_z value for g70/a30 was found to be significantly lower than that of other densities. The higher A_z values given with the DEDM technique proved better performance than those with the SEDM ($P < 0.001$). For example, in a breast thickness of 4.5 cm and with tissue densities of 50% glandular and 50% adipose (g50/a50), 5 same-sized microcalcifications with diameters of 0.39 and 0.16 mm were measured with the 2 techniques as shown in Figure 4. The SEDM technique had a tendency of overestimating diameter sizes of 0.39 mm and underestimating diameter sizes of 0.16 mm, respectively, leading to obtain worse detection accuracy compared with the DEDM technique.

DISCUSSION AND CONCLUSIONS

Computerized detection of microcalcifications has been at the forefront of research over the past decade. This study has shown that detection of microcalcifications depended not only on the signals present in the mammographic image but also on the limited contrast sensitivity of FFDM and image noise (tissue structure background), which clearly increased the FP detection rate. Using higher radiation exposure could be one of the methods to enhance contrast-to-noise ratios to improve bringing more microcalcifications to a visible level when the background is uniform. Nevertheless, a nonsignificant improvement in detecting microcalcifications might be achieved if complicated tissue structures were used. Thus, the anatomical noise would be the dominating factor that will limit visualization of microcalcifications.[19]

© 2012 Lippincott Williams & Wilkins

Copyright © 2012 Lippincott Williams & Wilkins. Unauthorized reproduction of this article is prohibited.

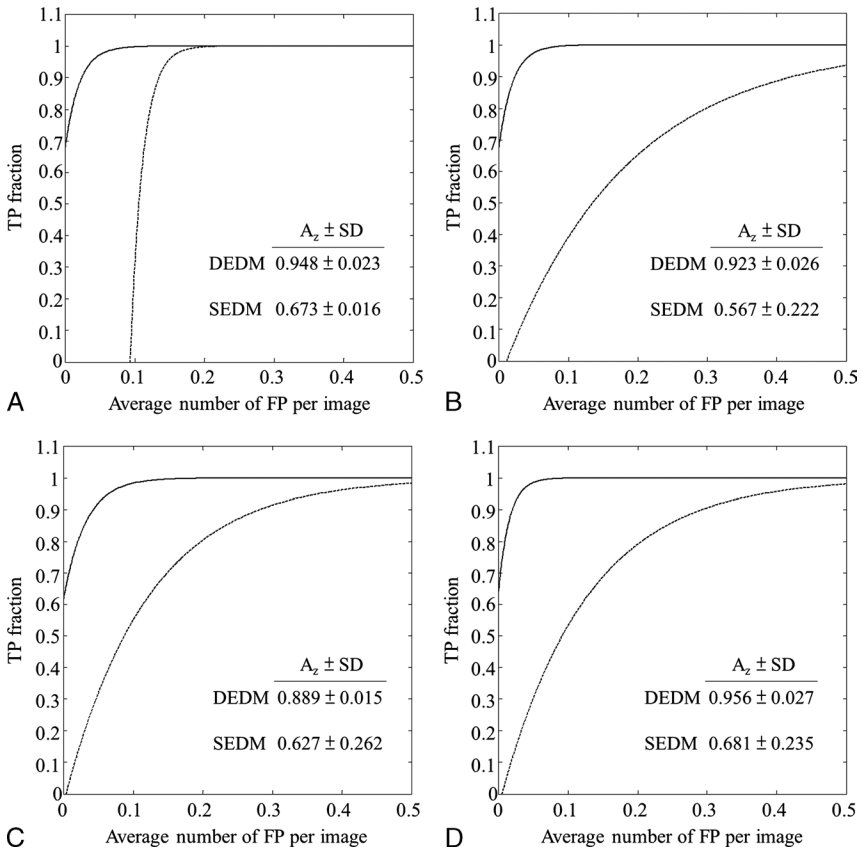

FIGURE 3. The FROC curves were obtained with both DEDM and SEDM techniques for tissue densities of g30/a70 (A), g50/a50 (B), g70/a30 (C), and overall performance (D), a combination of all tissue densities.

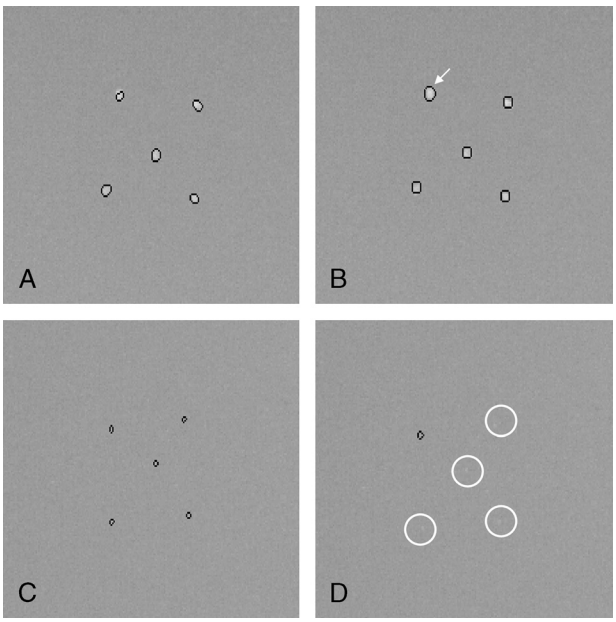

FIGURE 4. Images of 5 same-sized microcalcifications with diameters of 0.39 mm for DEDM (A), 0.39 mm for SEDM (B), 0.16 mm for DEDM (C), and 0.16 mm for SEDM (D) zoomed to display and measured under a compressed breast thickness of 4.5 cm with a tissue density of g50/a50.

In the study, we offer a DEDM model that simultaneously corrects for the inherently low contrast of microcalcifications and the high degree of noise in the subtracted image. The least detectable microcalcifications with our method were 0.2 mm, whereas the breast thickness was less than 5 cm, and the detectability could be further improved to 0.16 mm if breast

TABLE 3. Summary of Our Morphology and Measured A_z Values Compared With Other Research

Author	Morphology	A_z
Our experiment	Dual energy	0.89–0.95
Lado et al[21]	One-dimension wavelet transform	0.77 for fatty 0.64 for dense
Betal et al[22]	Top-hat and watershed algorithm	0.73–0.84
Hamid et al[23]	Real-valued and binary genetic algorithm	0.83–0.89
Papadopoulos et al[24]	Hybrid neural network classifier	0.91–0.92
Nakayama et al[25]	Filter bank	0.68–0.92
Yu et al[26]	Markov random field and fractal model	0.78–0.90
Ge et al[27]	Box-rim filter and FP reduction	0.95 for 10 iterations 0.99 for 90 iterations

© 2012 Lippincott Williams & Wilkins

Copyright © 2012 Lippincott Williams & Wilkins. Unauthorized reproduction of this article is prohibited.

thickness was less than 4.5 cm. These results demonstrated comparable sensitivities to other studies with FFDM (90% vs 92%) but a superior number of false-positives per image (0.019 vs 1.2).[20]

The area under the curves (A_z) in this study played a crucial rule for comparing detection accuracies, and our dual-energy technique obtained A_z values of 0.89 to 0.95, indicating a better detection accuracy compared with those of other studies,[21–26] with A_z values of approximately 0.83 to 0.91 using FFDM, and the comparisons were accordingly summarized in Table 3. In the study by Ge et al,[27] they obtained a detection accuracy with A_z values higher than 0.95, even up to 0.99, by using a series of complicated mathematical procedures and analyses, including inverted logarithm transforms, filtering, segmentations, convolution neural network, clustering, and linear discriminate analysis. However, their study was very time-consuming and required tremendous iterations to achieve such detection accuracy. Our proposed technique based on the dual-energy concept proved to be a better tradeoff between detection accuracy and computational burden.

For the past decade, a charge-coupled device–based slot scanning digital mammography (SSDM) has been developed and applied to breast imaging. Lai et al[19] have evaluated and compared the microcalcification detectability of 2 commercial digital mammography systems, SSDM and FFDM. Their study obtained an A_z value of 0.684 with FFDM, which was comparable to our experimental results with the SEDM (A_z = 0.681). In addition, they suggested that the SSDM was a better technique for detecting microcalcification than FFDM and that its accuracy could be increased when using a higher MGD (A_z values in SSDM vs FFDM: 0.753 vs 0.683 at 0.87 mGy and 0.836 vs 0.803 at 1.74 mGy, respectively). Nevertheless, under the same breast thickness of 5 cm in g50/a50 tissue density, our DEDM technique offered better detection accuracy (A_z = 0.923) compared with the SSDM, although MGD was 1.6 mGy for the DEDM (Table 4), slightly lower than the 1.74 mGy for the SSDM. However, the differences in MGD were not statistically significant.

There were not much differences in the MGDs with different tissue densities for the DEDM and the SEDM techniques, respectively, as shown in Table 4; however, the MGD increased with breast thickness owing to the need to increase the tube voltage and the tube current (Table 1). Our DEDM technique generally resulted in a higher MGD compared with that in the SEDM. However, a lower radiation dose could be possibly obtained for the DEDM technique with a thickness of less than 5 cm compared with that for the SEDM with thickness larger than 5 cm. Meanwhile, our DEDM technique could effectively detect microcalcifications sized up to 0.2 mm; thus, compression of the breast to a thickness of less than 5 cm was recommended to preserve the optimal microcalcification detection accuracy, with an effective benefit of minimizing the MGD.

The DEDM technique in this study was proposed to potentially provide more imaging information by using subtracted signals, instead of using logarithm image subtraction,[11–16] which would induce noise enhancement to lead rarely detectable microcalcifications. Although determination of the signal differences relying on accurate microcalcification measurement proved to be satisfactory, its classification of microcalcifications originated from the signal differences of microcalcifications with a size of 0.39 mm and from the background. In fact, it lacks slope information on equations (3) and (4), which were integrated signals of the high energy from E_2 to E_1, depending on the incident x-ray spectra and spatial nonuniformity of the x-ray intensity; detector response, in principle, could result in erroneous dual-energy imaging. Moreover, a higher kilovolt (peak) setting in high-energy imaging to enhance imaging contrast and further studies on mimicking the clinical situation more closely, likely useful in specimen projections, are also needed to collaborate with our findings. A classification system using the DEDM technique that could be incorporated in computer-aided detection to enhance the ability to interpret mammographic findings might be a topic for future research.

TABLE 4. Mean Glandular Dose Was Obtained at the 3 Tissue Densities With Thinner and Thicker Breast Thicknesses Using DEDM/SEDM Technique

		MGD, mGy		
Thickness, cm		**g30/a70**	**g50/a50**	**g70/a30**
Thinner	3	1.0/0.6	1.0/0.6	1.1/0.7
	3.5	0.9/0.6	1.1/0.7	1.1/0.7
	4	1.0/0.7	1.2/0.8	1.2/0.8
	4.5	1.2/0.9	1.4/1.0	1.5/1.1
Thicker	5	1.4/1.1	1.6/1.2	1.7/1.3
	6	1.9/1.5	2.3/1.8	2.5/2.0
	7	2.6/2.1	3.0/2.4	3.5/2.8

REFERENCES

1. Garfinkel L, Boring CC, Heath CW Jr. Changing trends: an overview of breast cancer incidence and mortality. *Cancer*. 1994;74:222–227.
2. Pisano ED. Current status of full field digital mammography. *Radiology*. 2000;214:26–28.
3. Williams MB, Fajardo LL. Digital mammography: performance considerations and current detector designs. *Acad Radiol*. 1996;3:429–437.
4. Fandos-Morera A, Prats-Esteve M, Tura-Soteras JM, et al. Breast tumors: composition of microcalcifications. *Radiology*. 1988;169:325–327.
5. Brettle DS, Cowen AR. Dual-energy digital mammography utilizing stimulated phosphor computed radiography. *Phys Med Biol*. 1994;39:1989–2004.
6. Wang TC, Karayiannis NB. Detection of microcalcifications in digital mammograms using wavelet. *IEEE Trans Med Imaging*. 1998;17:498–509.
7. Lemaur G, Drouiche K, DeConinck J. Highly regular wavelets for the detection of clustered microcalcifications in mammograms. *IEEE Trans Med Imaging*. 2003;22:393–401.
8. Davies DH, Dance DR. Automatic computer detection of clustered calcifications in digital mammograms. *Phys Med Biol*. 1990;35:1111–1118.
9. Lefebvre F, Benali H, Gilles R, et al. A fractal approach to the segmentation of microcalcifications in digital mammograms. *Med Phys*. 1995;22:381–390.
10. Netsch T, Peitgen HO. Scale-space signatures for the detection of clustered microcalcifications in digital mammograms. *IEEE Trans Med Imaging*. 1999;18:774–786.
11. Lewin JM, Isaacs PK, Vance V, et al. Dual-energy contrast-enhanced digital subtraction mammography: feasibility. *Radiology*. 2003;229:261–268.
12. Lemacks MR, Kappadath SC, Shaw CC, et al. A dual-energy subtraction technique for microcalcification imaging in digital mammography—a signal-to-noise analysis. *Med Phys*. 2002;29:1739–1751.

© 2012 Lippincott Williams & Wilkins

Copyright © 2012 Lippincott Williams & Wilkins. Unauthorized reproduction of this article is prohibited.

13. Ergun DL, Mistretta CA, Brown DE, et al. Single-exposure dual-energy computed radiography: improved detection and processing. *Radiology*. 1990;174:243–249.
14. Boone JM. Color mammography: image generation and receiver operating characteristic evaluation. *Invest Radiol*. 1991;26:521–527.
15. Kappadath SC, Shaw CC. Dual-energy digital mammography: calibration and inverse-mapping techniques to estimate calcification thickness and glandular-tissue ratio. *Med Phys*. 2003;30: 1110–1117.
16. Kappadath SC, Shaw CC. Dual-energy digital mammography for calcification imaging: scatter and nonuniformity corrections. *Med Phys*. 2005;32:3395–3408.
17. Carton AK, Bosmans H, Vandenbroucke D, et al. Quantification of Al-equivalent thickness of just visible microcalcifications in full field digital mammograms. *Med Phys*. 2004;31:2165–2176.
18. Cheng HD, Lui YM, Freimanis RI. A novel approach to microcalcification detection using fuzzy logic technique. *IEEE Trans Med Imaging*. 1998;17:442–450.
19. Lai CJ, Shaw CC, Geiser W, et al. Comparison of slot scanning digital mammography system with full-field digital mammography system. *Med Phys*. 2008;35:2339–2346.
20. McLoughlin KJ, Bones PJ, Karssemeijer N. Noise equalization for detection of microcalcification clusters in direct digital mammogram images. *IEEE Trans Med Imaging*. 2004;23:313–320.
21. Lado MJ, Tahoces PG, Méndez AJ, et al. A wavelet-based algorithm for detecting clustered microcalcifications in digital mammograms. *Med Phys*. 1999;26:1294–1305.
22. Betal D, Roberts N, Whitehouse GH. Segmentation and numerical analysis of microcalcifications on mammograms using mathematical morphology. *Br J Radiol*. 1997;70:903–917.
23. Hamid SZ, Farshid RR, Siamak PND. Comparison of multiwavelet, wavelet, Haralick, and shape features for microcalcification classification in mammograms. *Pattern Recognit*. 2004;37: 1973–1986.
24. Papadopoulos A, Fotiadis DI, Likas A. An automatic microcalcification detection system based on a hybrid neural network classifier. *Artif Intell Med*. 2002;25:149–167.
25. Nakayama R, Uchiyama Y, Yamamoto K, et al. Computer-aided diagnosis scheme using a filter bank for detection of microcalcification clusters in mammograms. *IEEE Trans Biomed Eng*. 2006; 53:273–283.
26. Yu SN, Huang YK. Detection of microcalcifications in digital mammograms using combined model-based and statistical textural features. *Expert Syst Appl*. 2010;37:5461–5469.
27. Ge J, Sahiner B, Hadjiiski LM, et al. Computer aided detection of clusters of microcalcifications on full field digital mammograms. *Med Phys*. 2006;33:2975–2988.

© 2012 Lippincott Williams & Wilkins

Copyright © 2012 Lippincott Williams & Wilkins. Unauthorized reproduction of this article is prohibited.